

# Key Factors of Stress Corrosion Cracking of X70 pipeline Steel in Simulated Deep-sea Environment: Role of Localized Strain and Stress

Yong Li<sup>1,2,&</sup>, Longfei Song<sup>1,2,&</sup>, Feilong Sun<sup>1,2,3,\*</sup>

<sup>1</sup> Corrosion and Protection Center, University of Science and Technology Beijing, Beijing, 100083, China

<sup>2</sup> Key Laboratory of Corrosion and Protection of Ministry of Education, Beijing, 100083, China

<sup>3</sup> China Building Material Test & Certification Group Co. Ltd., Beijing, 100024, China

<sup>&</sup>These authors contributed equally to this study and share first authorship,

\*E-mail: [1203407882@qq.com](mailto:1203407882@qq.com)

Received: 6 June 2018 / Accepted: 30 August 2018 / Published: 1 October 2018

---

The effect of the localized strain and stress on the stress corrosion cracking (SCC) of X70 steel in simulated seawater at 500 m depth was investigated by performing finite element analysis, electrochemical measurements, slow strain rate tensile (SSRT) tests, and scanning electron microscopy (SEM). The results suggested that the deformation accelerates the electrochemical reaction rate. The SCC susceptibility increases with the increase of elastic deformation, and it reaches the maximum value when stress strength increases to the yield point. In the plastic deformation, the deformation firstly increased then reduced SCC susceptibility because of hydrogen embrittlement (HE) and Bauschinger effect. The decrease of SCC susceptibility in plastic deformation was influenced by the increase of irreversible traps. It was observed that the cracks initiated at corrosion pits.

---

**Keywords:** deep sea environment; finite element analysis; mechanical electrochemistry; stress corrosion cracking

## 1. INTRODUCTION

Stress corrosion cracking (SCC) of pipeline steel has caused enormous destruction, especially in the harsh corrosive ocean environment [1]. Quite a few papers have reported that SCC is seriously affected by elastic and plastic deformation. Chen [2] found that the residual stress and tensile stress would accelerate corrosion and promote micropore formation. Gutman [3] concluded that deformation promoted the decrease in the metal electrode potential and the increase in the anode current. Parkins [4] demonstrated that the stress would seriously impact membrane rupture, pitting, and passivating, which

are directly related to crack nucleation and propagation. Moreover, Gao [5] indicated that the mechanical stress promoted the activity of the metal surface, accelerating the structural fracture. In addition, Lu [6] studied the effects of plastic deformation on X70 steel weld SCC susceptibility in a neutral solution, and proposed that plastic deformation reduces the SCC resistance in different areas of the X70 steel weld. Cui [7] investigated the influence of plastic deformation on the SCC behaviour of X70 steel and suggested that plastic deformation promoted cathodic reaction and hydrogen absorption and ingress into the steel and thus accelerated the SCC risk of X70 steel. Further, Ren [8] pointed out that no linear relationship exists between mechanical stress and electrochemical corrosion.

In an ocean environment, in addition to the variation in corrosive factors caused by variations in the depth, SCC is also affected by the plastic and elastic deformation. However, corrosive factors in the deep-sea environment are very different from those in shallow-sea and normal laboratory environments, which include high hydrostatic pressure, low dissolved oxygen, low pH under a corrosion product layer, and salinity [9, 10]. Some investigations [11, 12] have demonstrated the effect of hydrostatic pressure on metal and alloy corrosion: the rate of aluminium corrosion increases with the hydrostatic pressure and deeper pits are formed on 6061-T6 aluminium alloy, but generalized corrosion is inhibited due to the formation of a protective Mg-Al oxide layer. More recently, Yang [13, 14] et al. found that the pit growth rate increases with the increase in the hydrostatic pressure. Furthermore, low oxygen concentration and pH in the deep-sea environment may augment the hydrogen evolution reaction, which enhance fatigue cracking [15-18]. Some of the hydrogen atoms turn into the gas phase, while others are adsorbed on the electrode surface, which can penetrate the metal matrix [19], leading to hydrogen embrittlement (HE) [20]. Some studies suggested that hydrogen atoms are easily trapped in the steel with plastic deformation [21, 22]. Therefore, it is significant and urgent to study the effects of different degrees of deformation on the SCC behaviour and mechanical properties of pipeline steel.

It was pointed out that hydrostatic pressure may influence the SCC susceptibility of X70 steel by changing the permeated hydrogen concentration resulting from cathodic reaction [23], however, the SCC behaviour of pipelines with plastic and elastic deformation in deep-sea environments was not studied. In this work, the effects of varying elastic and plastic deformation on SCC behaviour and mechanical properties of X70 steel in a simulated deep ocean environment was investigated using electrochemical measurements, slow strain rate tensile (SSRT) tests, and scanning electron microscopy (SEM).

## 2. EXPERIMENTAL

### 2.1 Material

All specimens in this work were prepared from an API X70 pipe steel supplied by Nanjing Steel Co., China. The pipeline steel used in this study contains 0.045% C, 0.2% Si, 1.53% Mn, 0.013% P, 0.0036% S, 0.03% Cr, 0.15% Mo, 0.02% Ni, 0.048% V, 0.031% Cu and balance of Fe (by weight). The basic mechanical properties of the X70 pipeline steel are shown in Table 1.

**Table 1.** Mechanical properties of X70 pipeline steel

Elasticity modulus (GPa)	Poisson ratio	Yield strength (MPa)	Hardening coefficient	Hardening index	Tensile strength (MPa)	Elongation (%)	Reduction in-area (%)
210	0.30	482	2.18	20.63	562	44.6	87.6

2.2 Test environment

All experiments were carried out in the simulated environment of 500-m-depth seawater. The NaCl content in the solution was 3.5% in weight, and the solution pH was adjusted using NaOH to 7.5; further, the oxygen content was reduced to 2.6 mg/L by employing high-purity nitrogen gas flow. The hydrostatic pressure was 5 MPa achieved by using high-purity nitrogen, and the temperature was  $5 \pm 1^\circ\text{C}$ .

2.3 SSRT tests

SSRT tests were conducted on the LF-100-201-V-304 Test System produced by Termo Electron Corporation, USA. The specimens were prepared with dimensions shown in Fig. 1. Prior to testing, specimens were polished with 1500 grit emery paper with the burnishing direction parallel to the tension direction, and were then cleaned with deionized water and acetone. The different stresses in the elastic and plastic strain ranges were then applied, and the specimens were immersed in the simulated seawater for 24 h. Next, elastic deformation was applied at 0%, 40%, 72%, and 100% of the yield strength, and plastic deformation was achieved with 2%, 4.5%, 7.5%, and 12% of the applied plastic strain. Then, SSRT tests were performed at a strain rate of  $1.0 \times 10^{-6} \text{ s}^{-1}$ . Each test was repeated three times, and there was no discrepancy among the test results.

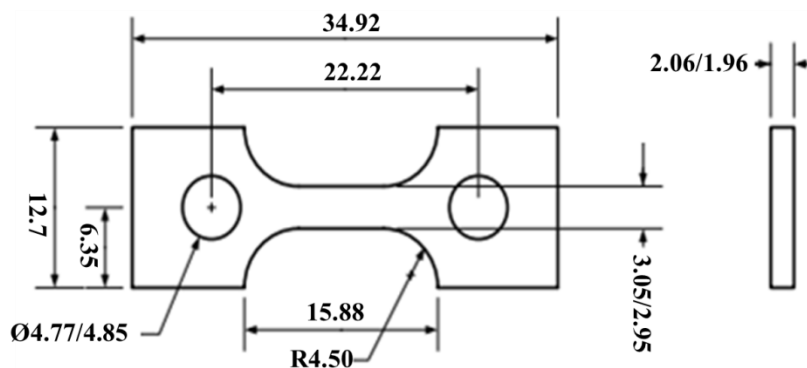


**Figure 1.** Sample for SSRT tests

The fracture surface of the specimens after SSRT tests was cleaned with deionized water and ethanol. The percentage of elongation and reduction in area of each specimen were measured, and after removing corrosion products, the fracture morphology was observed via SEM (Quanta250).

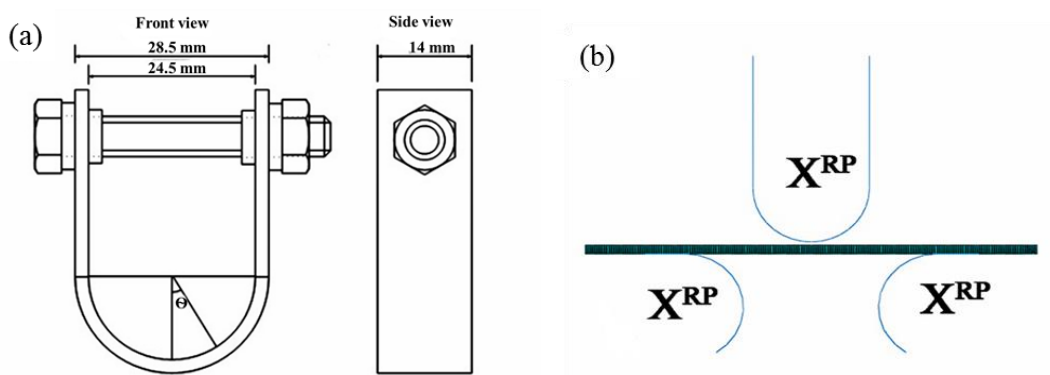
2.4 Analysis of stress and strain distributions

Fig. 2a shows the schematic diagram of U-specimens, which were prepared according to GB/T 15970.3. Both the stress and strain distribution of U-specimens were analyzed by using ABAQUS 6.10 software. Then, the electrochemical measurements with different deformation degrees were carried out on the selected area with varying stress and/or strain.

The finite element method was used to analyze stress and strain distributions of U-specimens by employing the ABAQUS 6.10 software. In the work, the length of the sample is 95 mm and thickness is 2 mm, as in the actual specimen. The mode was meshed with a CPS8R unit, the size of which was 0.5 mm, and the number of which was 760, as shown in Fig. 2b. The mechanical properties conformed to the constitutive relation [24, 25] was assumed by Eq. 1.

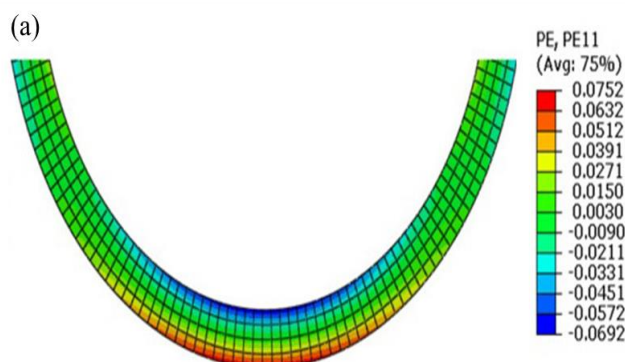
$$\varepsilon = \frac{\sigma}{E} + \alpha \frac{\sigma_0}{E} \left( \frac{\sigma}{\sigma_0} \right)^n \tag{1}$$

Here,  $\sigma$  and  $\varepsilon$  are the stress and strain, respectively, and  $\sigma_0$ ,  $\alpha$ , and  $n$  are the yield strength, hardening coefficient, and hardening index, respectively.



**Figure 2.** The schematic diagram of U-specimens (a) and finite element model and the sample grid (b)

The distance between the underdraught head and sample surface was 0.75 mm, as shown in Fig. 2b. The underdraught head was pushed down by 0.752 mm to establish a stable contact with the sample to avoid convergence in the calculation process. Then, the underdraught head was pushed down by 30 mm to prepare the U-specimen according to GB/T 15970.3. The finite element software was used to analyze the stress and strain distributions of U-specimens.



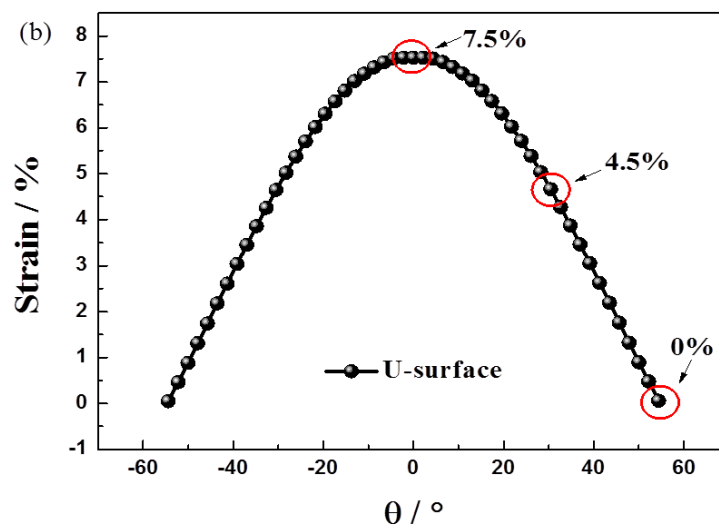


**Figure 3.** Plastic strain distribution of the U-specimen (a) and distribution of the plastic strain of the U-specimen outer surface with the change in the angle (b)

Fig. 3a shows the plastic strain distribution of the U-specimen. It is seen that the maximum plastic strain appears in the top of the U-specimen outer surface and is up to 7.52%. Then, a gradual decrease follows with the increase in the distance from the top. In order to mark the position in the arc of the U-specimen, the arc centre of the U-specimen was used as the center of the circle, with the angle ( $\theta$ ) of the top  $0^\circ$ , right is positive angle, left is negative angle, as shown in Fig. 2a. The distribution of the plastic strain of the U-specimen outer surface with the change in the angle is shown in Fig. 3b.

### 2.5 Electrochemical measurement

The U-specimen was polished subsequently to 1500 grit emery papers with the direction parallel to the tensile stress direction, and then cleaned with acetone. The U-specimen was sealed with silicone rubber, with a working area of  $0.5 \text{ cm}^2$  exposed to 0%, 4.5%, and 7.5% of the plastic strain of the U-specimen outer surface according to the results of finite element analysis (Fig. 3).

Electrochemical measurements were carried out using a GAMRY Instruments Reference 3000 electrochemical work station connected to a three-electrode system, where the exposed part of the U-specimen, a platinum plate, and a Ag/AgCl electrode (containing 1 mol/L KCl) was used as the working electrode, counter electrode, and reference electrode, respectively. The reference electrode potential of the Ag/AgCl electrode was 0.222 V vs. standard hydrogen electrode (SHE). All the measured potentials in the study were converted to the values relative to SHE. The pressure of the test environment was controlled to 5 MPa using high-purity nitrogen in an autoclave. The temperature was controlled for  $5 \pm 1^\circ\text{C}$  by using a water bath.

The potentiodynamic polarization measurement was performed from  $-0.25 \text{ V}$  to  $1.6 \text{ V}$  vs. the open circuit potential (OCP), with a potential scanning rate of  $0.333 \text{ mV/s}$ . Electrochemical impedance spectroscopy (EIS) was performed at the OCP with the alternating current voltage disturbance of  $10 \text{ mV}$ , within a frequency ranging from 100000 to  $0.01 \text{ Hz}$ .

All the tests in the work were carefully carried out in triplicate to assure the reproducibility and

reliability of the results.

### 3. RESULTS AND DISCUSSION

#### 3.1 SSRT with the different deformation

SSRT curves obtained after immersion tests for 24 h under varying elastic prestrain values are shown in Fig. 4. It was found that the tensile strength of the X70 steel pipe gradually increased, and the elongation decreased as the elastic prestrain increased from 0% to 100%  $\sigma_s$  (yield strength). The results above indicate that the elastic prestrain increases the SCC susceptibility of X70 steel pipe in the simulated solution.

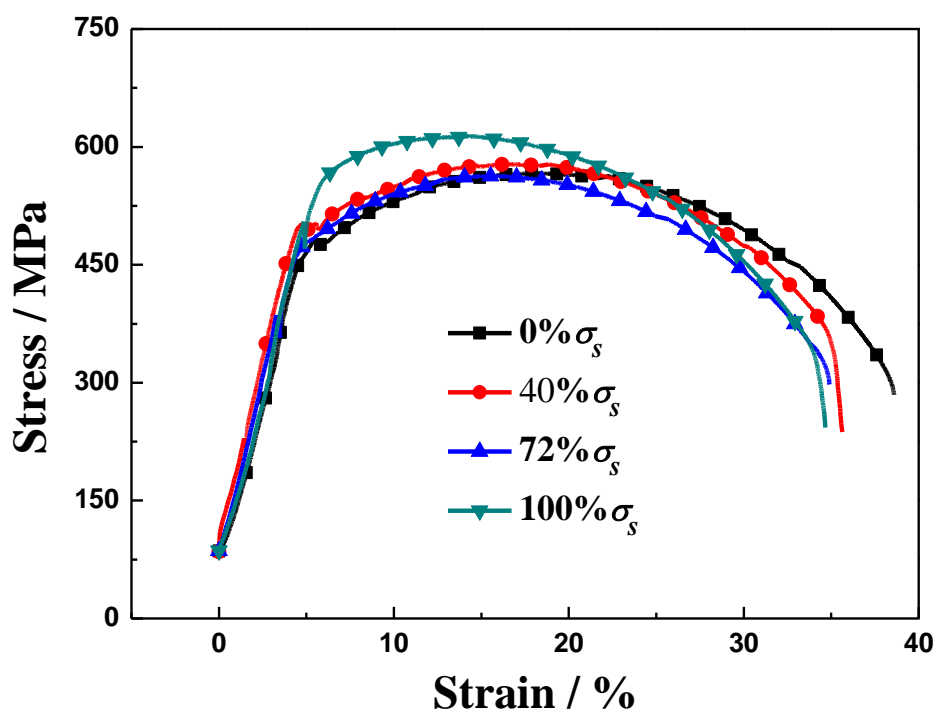


**Figure 4.** SSRT curves of X70 steel with different elastic deformation in artificial seawater

Fig. 5 shows SSRT curves with different plastic deformation (0.35%, 2%, 4.5%, 7.5%, and 12% of the original length of the sample extension area) obtained after immersion in 500-m-depth simulated seawater for 24 h. It can be concluded that the strength with the plastic deformation at yield point for 24 h is maximum, and the elongation is minimum. Then, the strength increases after a decreasing stage, and the elongation presents the opposite trend. The strength of the X70 steel specimen with 4.5% plastic deformation is minimum, and the elongation is maximum.

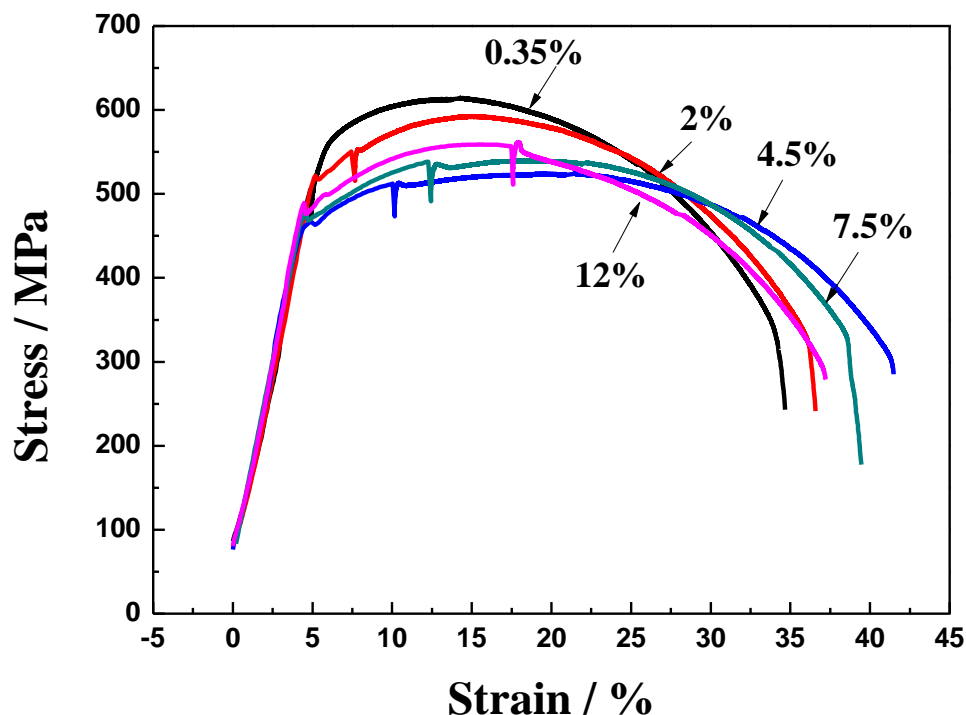


Figure 5. Stress-strain curves of X70 steel with different plastic deformation in artificial seawater

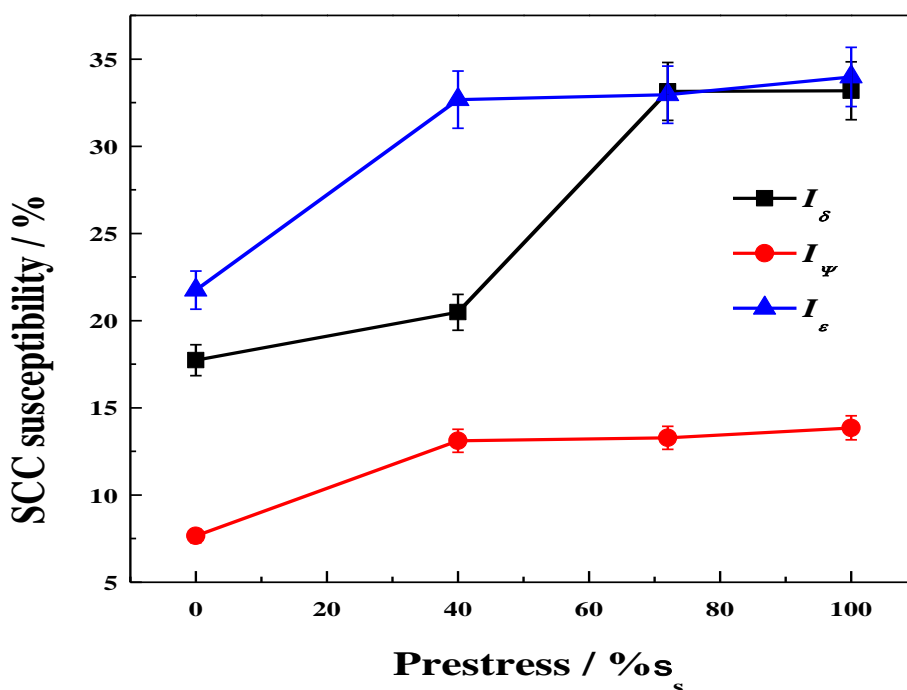


Figure 6. SCC susceptibility of X70 steel with different plastic deformation with different elastic deformation in artificial seawater

In order to analyze the effect of the prestrain values on the SCC property, the rate of the elongation-loss rate ( $I_\delta$ ), the reduction loss in area ( $I_\psi$ ) and fracture strength loss ( $I_\epsilon$ ) were calculated to quantify the SCC susceptibility. These are defined as follows [26]:

$$I_{\delta} = \left(1 - \frac{\delta_s}{\delta_0}\right) \times 100\% \quad (2)$$

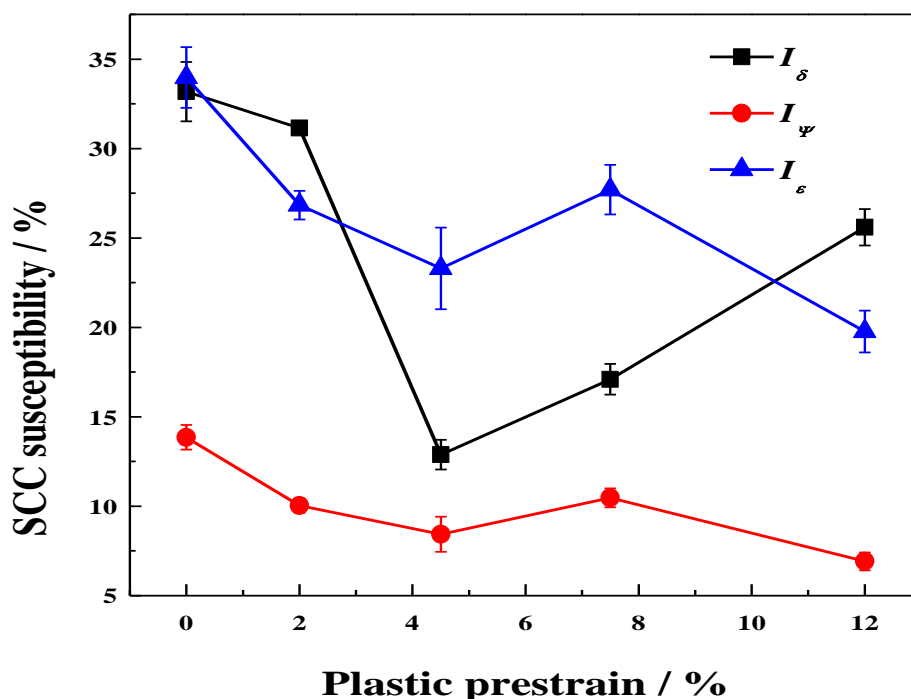
$$I_{\Psi} = \left(1 - \frac{\Psi_s}{\Psi_0}\right) \times 100\% \quad (3)$$

$$I_{\epsilon} = \left(1 - \frac{\epsilon_s}{\epsilon_0}\right) \times 100\% \quad (4)$$

Here,  $\delta_0$ ,  $\Psi_0$  and  $\epsilon_0$  are the elongation, reduction in area and fracture strength measured with different plastic deformation in air, respectively, and  $\delta_s$ ,  $\Psi_s$  and  $\epsilon_s$  are the elongation, reduction in area and fracture strength measured with different plastic deformation in simulated sea environment, respectively. With the same deformation,  $I_{\delta}$  was calculated by  $\delta_0$  and  $\delta_s$ , and  $\Psi_0$  and  $\epsilon_0$  were calculated in the same way.

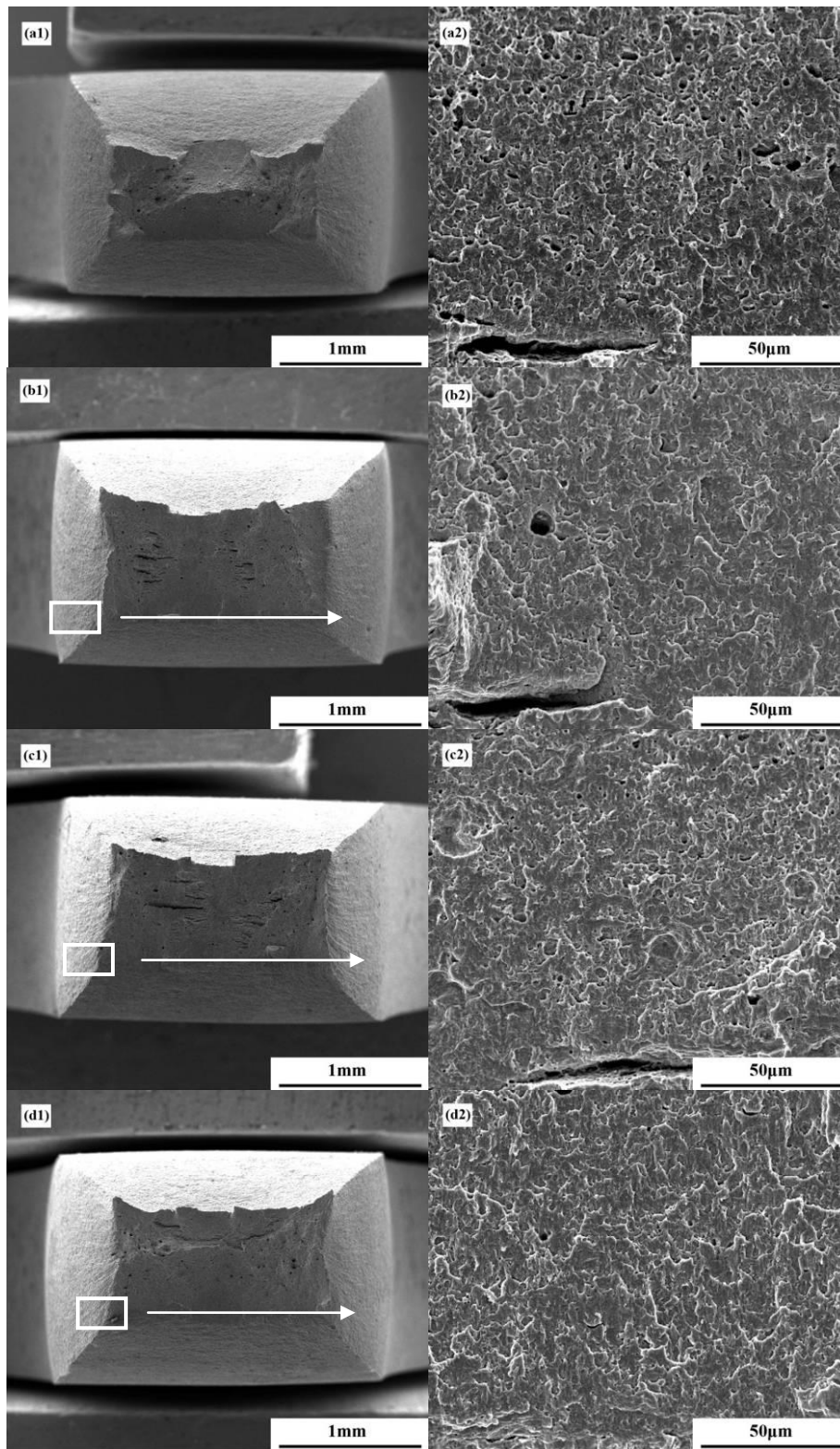
As shown in Fig. 6,  $I_{\delta}$ ,  $I_{\Psi}$  and  $I_{\epsilon}$  increase gradually with increasing elastic deformation, where  $\sigma_s$  is the yield strength. The maximum  $I_{\delta}$ ,  $I_{\Psi}$  and  $I_{\epsilon}$  corresponds to the maximum elastic deformation (yield strength point), i.e., the largest SCC susceptibility.

The curves of SCC susceptibility versus plastic deformation are shown in Fig. 7. The change trends of  $I_{\delta}$ ,  $I_{\Psi}$ , and  $I_{\epsilon}$  are not exactly the same. The curve of  $I_{\Psi}$  shows a slight fluctuation with the increase in the plastic deformation degree, reaching the maximum and minimum values with the plastic deformation applied 0.35% and 4.5% of the original length, respectively. The curves of  $I_{\delta}$  and  $I_{\epsilon}$  fluctuate greatly with the maximum values obtained for 0.35% plastic deformation, and the minimum values obtained for the plastic deformation applied 12% of the original length. However, the maximum value of SCC susceptibility of X70 steel pipe appears with the plastic deformation applied 0.35% of the original length.

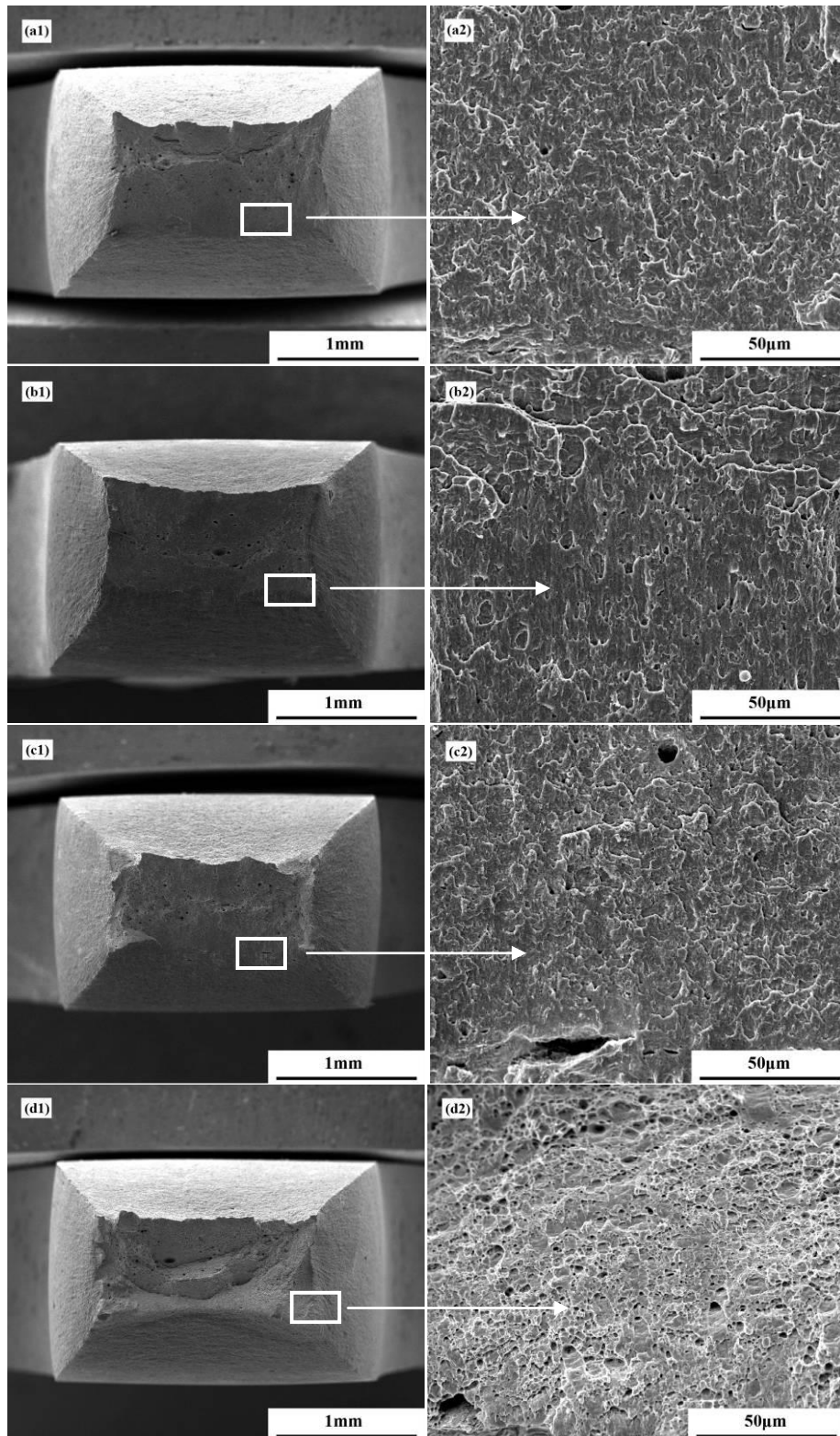


**Figure 7.** The SCC susceptibility of X70 steel with different plastic deformation in artificial seawater

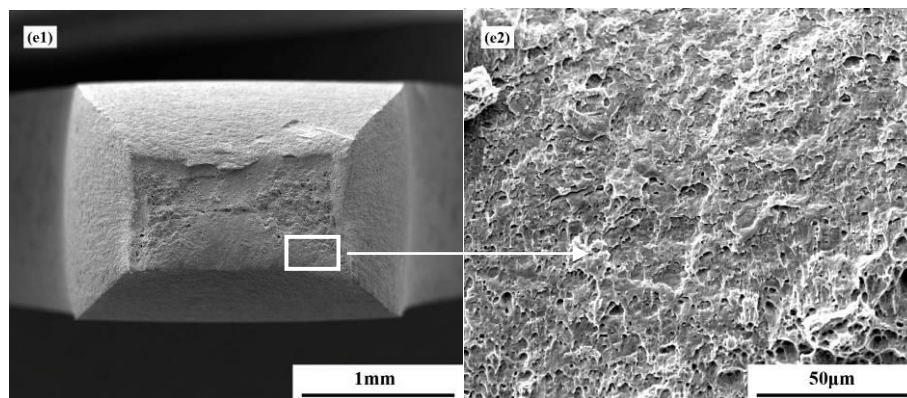
3.2 SEM images of fracture surfaces after SSRT tests with different degrees of deformation



**Figure 8.** SEM images of fracture surfaces of X70 steel after SSRT tests with different elastic deformation in artificial seawater ((a) 0%, (b) 40%, (c) 72%, (d) 100% of the yield strength)



**Figure 9.** The SEM images of fracture surfaces of X70 steel after SSRT tests with different plastic deformation ((a) 0.35%, (b) 2%, (c) 4.5%, (d) 7.5%, and (e) 12% of the original in artificial seawater



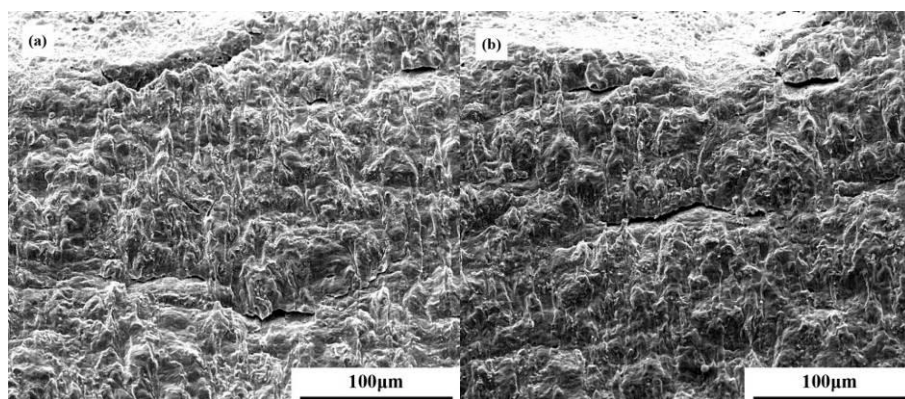
**Figure 9.** (Continued)

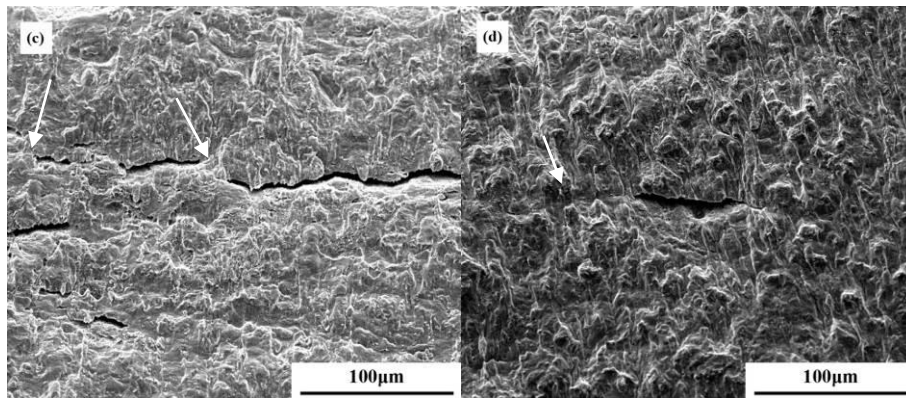
Fig. 8 shows the SEM images of fracture surfaces after the SSRT tests with different degrees of elastic deformation. Extensive necking of the macro fracture without deformation (Fig .8a) is observed. The necking degree decreases gradually, and fracture surface becomes smoother with increasing elastic deformation, as shown in Figs .8a to 8d. Further, the enlargement of the brittle fracture area and the decline of dimples were observed on the fracture, as shown in Figs .8a to 8d. It could be concluded that the increase in the elastic deformation degree enhances the SCC susceptibility of the X70 steel pipe in the simulated solution.

Both tensile and compression stress enhanced the surface electrochemical activity [27]. The increase in the stress leads to a decrease in the electrode potential, resulting in the easy generation of hydrogen atoms. HE leads to the presence of brittle fracture at the fracture surface in Fig. 8. Moreover, the material surface activity increases continuously with increasing deformation [28].

Thus, the deformation caused by the applied tensile stress increases the probability of hydrogen atoms penetrating the metal, which results in increasing SCC susceptibility. This result is consistent with the result shown in Figs. 4 and 6. Thus, the process was mainly affected by HE.

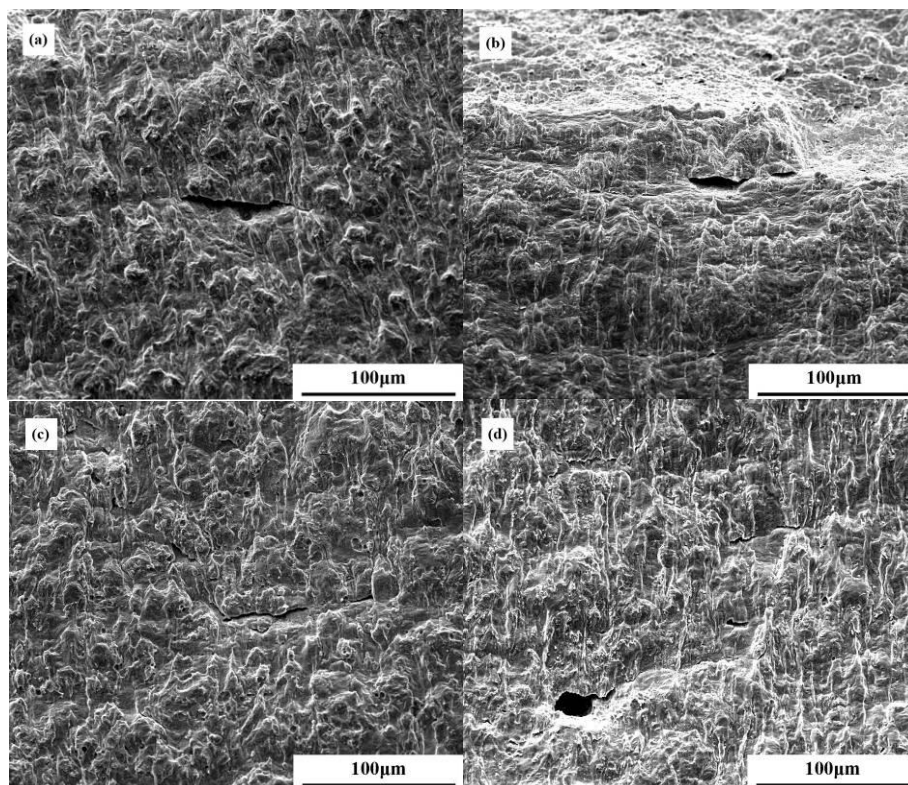
The SEM images of fracture surfaces after SSRT tests with different plastic deformation are shown in Fig. 9. It can be seen that there are obvious necking at all macroscopic fractures, with brittle fracture surface and some dimples at edge of the fractures. The fracture in the case of the plastic deformation at yield point is smoothest, and brittle fracture characteristic is most obvious.





**Figure 10.** SEM images of the fracture side surfaces of X70 steel after the SSRT tests with different degrees of elastic deformation in artificial seawater ((a) 0%, (b) 40%, (c) 72%, and (d) 100% of the yield strength)

The SEM images of the fracture side surfaces of X70 steel pipe specimen after SSRT tests with different degrees of elastic deformation are as shown in Fig. 10. The transverse crack extension direction was approximately linear, without twists and turns along the grain boundary, which implied that the crack extension is transgranular. However, the microcracks size of the specimen without deformation was smaller, indicating that the number and the size of microcracks on the fracture side surfaces increased with an increase in the degree of elastic deformation.



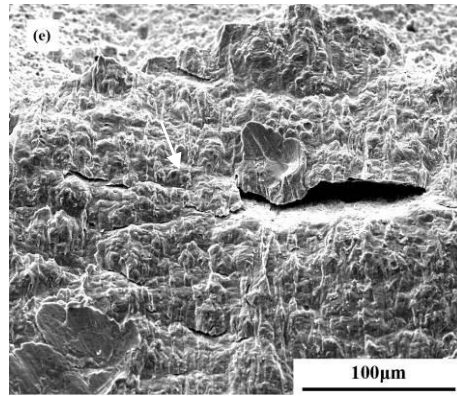


**Figure 11.** SEM images of fracture side surfaces after SSRT tests with different degrees of plastic deformation in artificial seawater ((a) yield strength, (b) 2%, (c) 4.5%, (d) 7.5%, (e) 12% of the original length)

Fig. 11 shows the SEM images of the fracture side surfaces of the X70 steel pipe specimen after the SSRT tests with different degrees of plastic deformation. It is seen that there are microscopic cracks on the fracture side surfaces, and their size is larger in the X70 steel specimens subjected to plastic deformation of 0.35% and 12% of the original length. Large numbers and big size of microscopic cracks on the surface of the metal would decrease mechanical property of the specimen, accelerating the fracture.

It can be observed that the variation of  $I_{\delta}$ ,  $I_{\psi}$ , and  $I_{\epsilon}$  (Fig. 6) in elastic prestrain is not conform to the variation in plastic deformation (Fig. 7). The reason is that hydrogen atoms are easily trapped by irreversible traps in the steel with plastic deformation [21, 22], resulting in the decrease of hydrogen atoms number in reversible traps, which enhance the crack propagation with hydrogen moving to the crack tip[29]. When deformation reaches to 8%, exceed the tensile strength point,  $I_{\delta}$ ,  $I_{\psi}$ , and  $I_{\epsilon}$  increase by the effect of Bauschinger effect. As a whole, the HE effect is inhibited with the increase of plastic deformation, which is consistent with the results in Fig. 9.

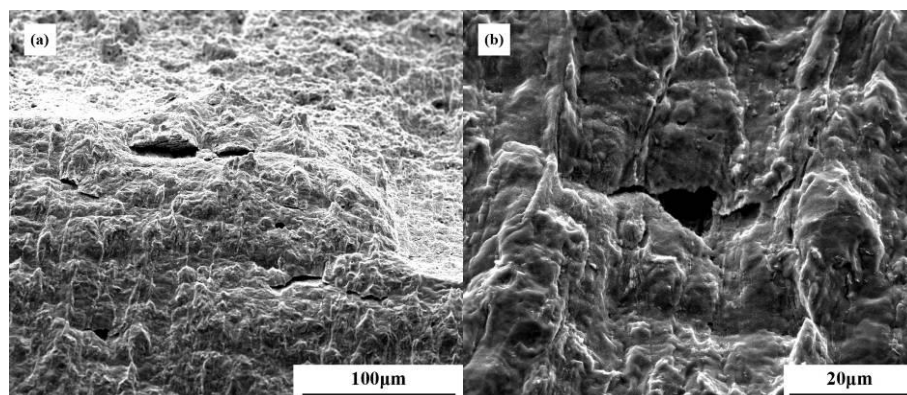


**Figure 12.** SEM images of fracture side surfaces of X70 steel after SSRT tests with elastic deformation in artificial seawater (100% of the yield strength)

The microcrack size of the specimen with the deformation at yield point was larger. Some microcracks through corrosion pitting were observed, as shown in Fig. 12. This implied that the cracks

initiated at corrosion pits.

### 3.3 Electrochemical behaviour

Fig. 13 shows the difference in the anode polarization curves of X70 steel pipe U-specimens with 0%, 4.5%, and 7.5% plastic deformation in the 500-m-depth simulated seawater. It is seen that the anode polarization curves' slope is highest without plastic deformation, and the slope gradually decreases as the degree of plastic deformation increases; this illustrates that plastic deformation enhances the rate of anodic dissolution reaction.

Plastic deformation plays an important role in promoting the cathodic and anodic reactions of pipe line steel [30, 31]. The corrosion resistance is affected by the surface activity and dislocation structure [32]. Surface defects caused by the synergistic effect of stress and the electrochemical process in the strain process, result in an increase in the local potential, which promotes the electrode reaction [33]. The plastic deformation is proportional to the number of vacancies and dislocation [28]. Increasing number of vacancies and dislocation increase the microcosmic electrochemical activity, which accelerates the rate of anode dissolution and leads to a higher macroscopic electrochemical activity. This indicates that there is an inversely proportional relationship between the electrochemical reaction resistance and plastic deformation, which accelerates the corrosion rate of X70 steel pipe.

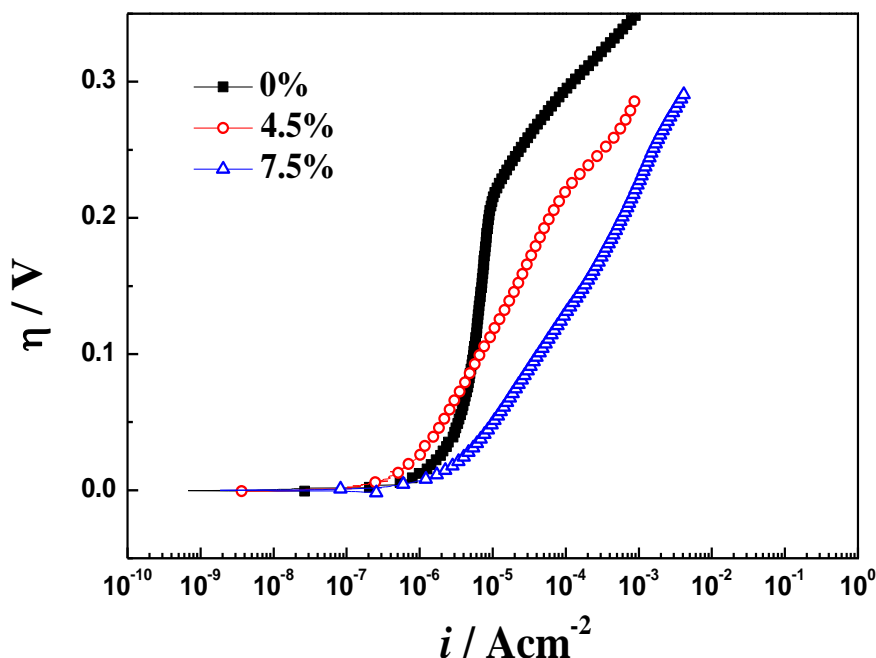


**Figure 13.** Anode polarization curves of X70 steel with the plastic deformation in artificial seawater

Fig. 14 shows the electrochemical impedance spectroscopy (EIS) curves of X70 steel pipe U-specimens with plastic deformation of 0%, 4.5%, and 7.5% in simulated seawater. It can be concluded that the low-frequency impedance modulus in the simulated solution decreases with an increase in the plastic deformation degree, which indicates that the corrosion resistance decreases.

**Table 2.** EIS analysis results with different plastic deformation

Plastic deformation/%	$E_{corr}/V_{SCE}$	$i_{corr}/A\ cm^{-2}$	$R_f/\Omega\ cm^2$	$R_t/\Omega\ cm^2$	$R_p/\Omega\ cm^2$
0	-0.540	$1.04 \times 10^{-6}$	760	19910	20670
4.5	-0.582	$2.14 \times 10^{-6}$	1979	13913	15892
7.5	-0.601	$3.99 \times 10^{-6}$	3308	4854	8162

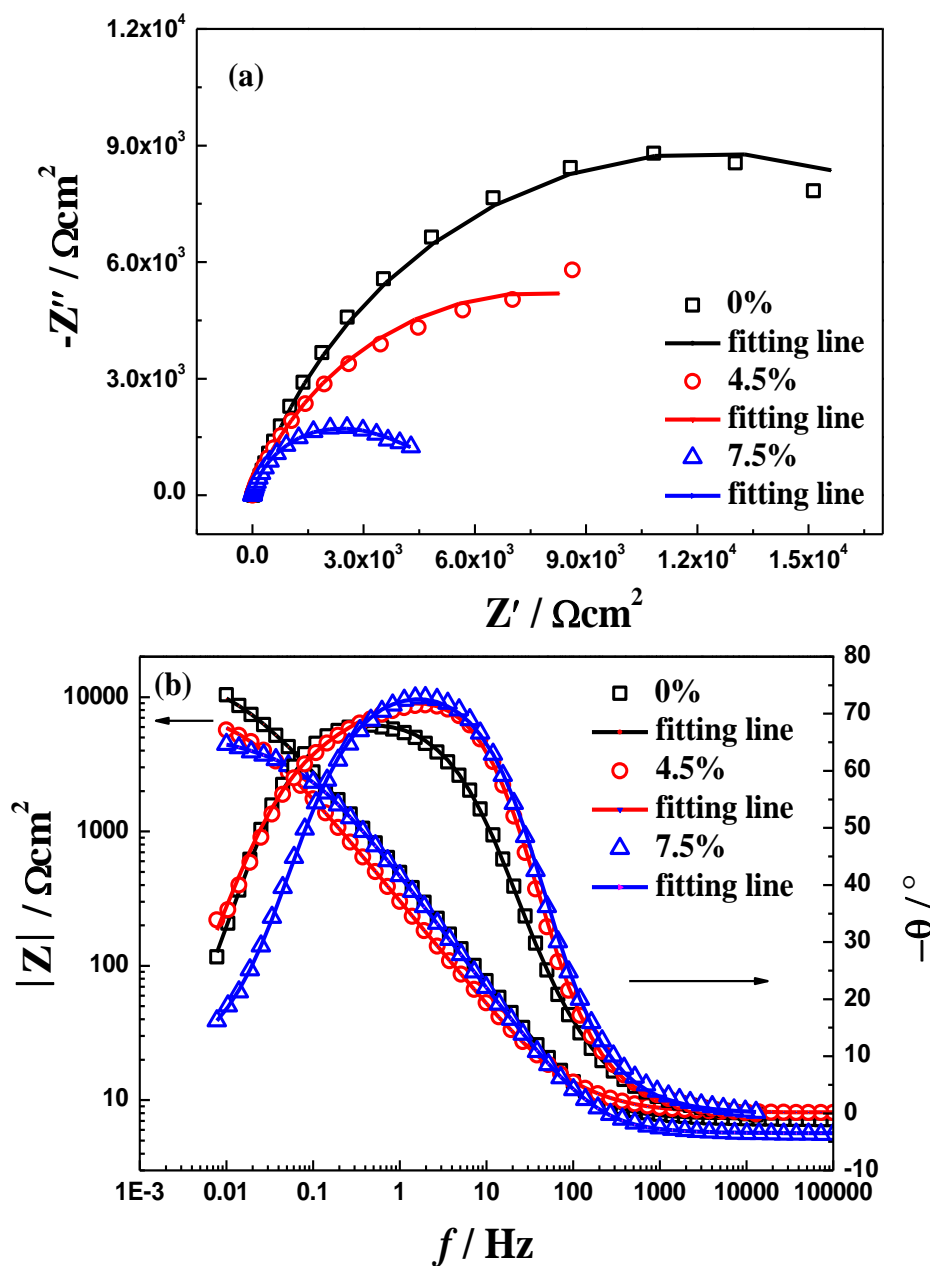


**Figure 14.** Nyquist graph (a) and Bode diagram (b) of specimens of X70 steel with the plastic deformation in artificial seawater

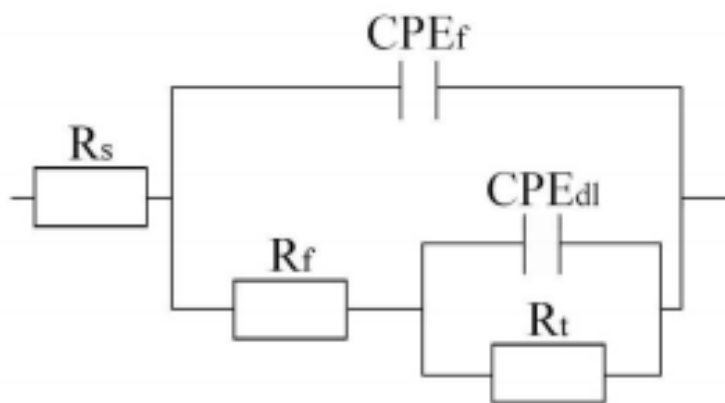
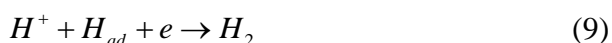
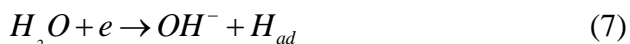


**Figure 15.** Equivalent circuit

EIS data were fitted with the ZSimpWin software and the equivalent circuit is obtained, as shown in Fig. 15.  $R_t$  is the charge-transfer resistance,  $R_f$  is corrosion products film resistance,  $R_s$  is the solution resistance between the reference and working electrodes,  $CPE_f$  is the corrosion products film capacitance, and  $CPE_{dl}$  is electrical double-layer capacitor [34-37].

Table 2 displays kinetic parameters and the EIS analysis results for the X70 steel pipe specimens with different plastic deformation, where the polarization resistance  $R_p = R_f + R_t$ .  $R_p$  gradually decreases as the degree of plastic deformation increases, which illustrates that corrosion tends to increase with increasing plastic deformation.

Because of the low oxygen content (2.6 mg/L) in the deep-sea environment, the cathode reaction is mainly the hydrogen evolution reaction, divided into three steps [16, 38]:



This mechanism boosts the generation of hydrogen atoms. The low pH in the deep-sea further increases the number of hydrogen atoms. It can be inferred that plastic deformation enhances the anodic dissolution of X70 steel pipe, and the corrosion rate increases as the plastic deformation degree increases. This is because the dislocation density increases with the deformation degree, which leads to dislocation pileup. The formation of the dislocation pileup increases the inner stress and leads to the increase in the flow stress, which in turn cause material strengthening. With the increase in the number of dislocations in the dislocation pileup formed around barriers in the process of deformation strengthening, the partial equilibrium potential around dislocations decreases, which leads to an increase in the anode dissolution rate [39].

#### 4. CONCLUSIONS

The SCC susceptibility of the X70 steel pipe in deep seawater increases with the increase in the elastic pre-strain, and reaches the maximum value at the yield strength point, due to the increase of HE effect. Under the plastic pre-strain conditions, the increase of deformation (0.35% to 4%) decreases the SCC susceptibility resulting from the decrease of the effect of HE. As the plastic deformation exceeds tensile strength point, the SCC susceptibility firstly increases then decreases, because of Bauschinger

effect.

Electrochemical reaction rate is promoted by the increase of deformation, while the SCC susceptibility does not increase monotonously with increasing deformation in the plastic zone. This is attributed to the effect of dislocations that generated during plastic deformation on the hydrogen trap. Thus, HE plays an important role in SCC of the X70 steel pipe in deep seawater.

#### ACKNOWLEDGEMENTS

This study is supported by the National Environmental Corrosion Platform (NECP), the National Basic Research Program of China (973 Program project, No. 2014CB643300), and the National Natural Science Foundation of China (No. 51471034).

#### References

1. X. Li, D. Zhang, Z. Liu, Z. Li, C. Du, C. Dong, *Nature*, 527 (2015) 441.
2. W. Chen, G. Van Boven, R. Rogge, *Acta Mater.*, 55 (2007) 43.
3. E. Gutman, G. Solovioff, D. Eliezer, *Corros. Sci.*, 38 (1996) 1141.
4. R.N. Parkins, CORROSION 2000, NACE International, 2000.
5. K. Gao, D. Li, X. Pang, S. Yang, *Corros. Sci.*, 52 (2010) 3428.
6. B. Lu, J.-L. Luo, D.G. Ivey, *Metall. Mater. Trans. A*, 41 (2010) 2538.
7. Z. Cui, Z. Liu, L. Wang, X. Li, C. Du, X. Wang, *Mater. Sci. Eng. A*, 677 (2016) 259.
8. R. Ren, S. Zhang, X. Pang, K. Gao, *Electrochim. Acta*, 85 (2012) 283.
9. S. Chen, W. Hartt, S. Wolfson, *Corrosion*, 59 (2003) 721.
10. A. Cheng, N.-Z. Chen, *Ocean Eng.*, 142 (2017) 10.
11. A. Beccaria, G. Poggi, G. Castello, *Br. Corros. J.*, 30 (1995) 283.
12. B. Liu, T. Zhang, Y. Shao, G. Meng, J. Liu, F. Wang, *Int. J. Electrochem. Sci.*, 7 (2012) 1864.
13. Y. Yang, T. Zhang, Y. Shao, G. Meng, F. Wang, *Corros. Sci.*, 52 (2010) 2697.
14. Y. Yang, T. Zhang, Y. Shao, G. Meng, F. Wang, *Corros. Sci.*, 73 (2013) 250.
15. J. Xiao, S. Qiu, Y. Chen, Z. Lin, Q. Xu, H. Xie, *Int. J. Fatigue*, 74 (2015) 65.
16. G. Meng, F. Sun, S. Wang, Y. Shao, T. Zhang, F. Wang, *Electrochim. Acta*, 55 (2010) 2238.
17. Z. Cui, S. Chen, L. Wang, C. Man, Z. Liu, J. Wu, X. Wang, S. Chen, X. Li, *J. Electrochem. Soc.*, 164 (2017) C856.
18. Y. Li, *Int. J. Electrochem. Sci.*, 11 (2016) 5021.
19. Z. Liu, X. Li, C. Du, L. Lu, Y. Zhang, Y. Cheng, *Corros. Sci.*, 51 (2009) 895.
20. P. Traverso, E. Canepa, *Ocean Eng.*, 87 (2014) 10.
21. S.J. Kim, D.W. Yun, D.W. Suh, K.Y. Kim, *Electrochem. Commun.*, 24 (2012) 112.
22. A.-M. Brass, J. Chêne, *Corros. Sci.*, 48 (2006) 481.
23. F. Sun, S. Ren, Z. Li, Z. Liu, X. Li, C. Du, *Mater. Sci. Eng. A*, 685 (2017) 145.
24. W. Ramberg, W.R. Osgood, Description of stress-strain curves by three parameters, (1943).
25. A. De Martino, R. Landolfo, F. Mazzolani, *Mater. Struct.*, 23 (1990) 59.
26. L. Wang, L. Cheng, J. Li, Z. Zhu, S. Bai, Z. Cui, *Materials*, 11 (2018) 465.
27. L. Nation, J. Li, C. James, Y. Qi, N. Dudney, B.W. Sheldon, *J. Power Sources*, 364 (2017) 383.
28. X. Feng, X. Lu, Y. Zuo, D. Chen, *Corros. Sci.*, 82 (2014) 347.
29. M. Mohtadi-Bonab, J. Szpunar, L. Collins, R. Stankievech, *Int. J. Hydrogen Energy*, 39 (2014) 6076.
30. L. Xu, Y. Cheng, *Corros. Sci.*, 64 (2012) 145.
31. L. Xu, Y. Cheng, *Corros. Sci.*, 59 (2012) 103.
32. B. Lu, H. Yu, J. Luo, *J. Mater. Eng. Perform.*, 22 (2013) 1430.

33. Z. Liu, X. Li, C. Du, G. Zhai, Y. Cheng, *Corros. Sci.*, 50 (2008) 2251.
34. H. Qian, D. Xu, C. Du, D. Zhang, X. Li, L. Huang, L. Deng, Y. Tu, A.J.M.C. Mol, H. Terryn, *J. Mater. Chem. A*, 5 (2017) 2355-2364.
35. L. Wang, L. Deng, D. Zhang, H. Qian, C. Du, X. Li, J.M.C. Mol, H.A. Terryn, *Prog. Org. Coat.*, 97 (2016) 261.
36. D. Zhang, H. Qian, L. Wang, X. Li, *Corros. Sci.*, 103 (2016) 230.
37. D. Zhang, L. Wang, H. Qian, X. Li, *J. Coat. Technol. Res.*, 13 (2016) 11.
38. G. Meng, C. Zhang, Y. Cheng, *Corros. Sci.*, 50 (2008) 3116.
39. M. Rifai, E. Bagherpour, G. Yamamoto, M. Yuasa, H. Miyamoto, *Adv. Mater. Sci. Eng.*, 2018 (2018).

© 2018 The Authors. Published by ESG ([www.electrochemsci.org](http://www.electrochemsci.org)). This article is an open access article distributed under the terms and conditions of the Creative Commons Attribution license (<http://creativecommons.org/licenses/by/4.0/>).